Geomech. Geophys. Geo-energ. Geo-resour. (2020)6:48
https://doi.org/10.1007/s40948-020-00172-y

ORIGINAL ARTICLE

Porosity and permeability of the overburden from wireline logs: a case study from offshore Malaysia

José M. Carcione · Davide Gei · Stefano Picotti · M. Shahir Misnan · M. Rashad Amir Rashidi · Zainol Affendi Abu Bakar · Zuhar Zahir Tuan Harith · Nabila Hannah Samsol Bahri · Noorbaizura Hashim

Received: 8 October 2019 / Accepted: 9 July 2020

Abstract In the framework of a CO_2 storage feasibility study, we evaluate porosity and permeability of shale formations constituting the overburden of a hydrocarbon reservoir, where the gas is stored. These properties are required to perform fluid-flow simulations and analyze possible leakages from the reservoir to the surface. In this process, calibration with well logs is essential. Standard log-interpretation procedures on shales may induce errors, since the shale part is discarded due to its apparent negligible permeability compared to the clastic part. In this study, it is the "shale effect" that we consider by introducing its contribution to porosity and therefore to permeability, so that new expressions are developed to obtain porosity from density and traveltimes that consider this effect. Indeed, shales have non-zero porosity and finite permeability even if the flow rates are several orders of magnitude smaller than those in sandstones. Moreover, calibration does not mean to honour one single log profile but the interpretation should be compatible with all the profiles available. We obtain clay content, porosity and permeability from two wells offshore Malaysia using the linear and Stieber relations between gamma ray and shale volume. The results of using these relations are quite similar. However, the analysis shows that the density logs yield too small values of porosity. Instead, the sonic log gives a better estimate of porosity that honours the P-wave velocity. The verification is performed by using the Krief–Gassmann equations to obtain the P-wave velocity, either from the density-log or from sonic-log derived porosities. This is also confirmed by comparison to porosity obtained from the neutron log.

Keywords Porosity · Permeability · Well logs · Overburden · CO_2 storage

1 Introduction

The emission of carbon dioxide (CO_2) to the atmosphere is a serious climate issue. Storing this gas into the subsurface is one of the possible solutions. Storage is currently taking place all around the world, such as the large commercial-scale projects Sleipner in Norway and Weyburn-Midale in Canada (Brown et al. 2017). These activities demonstrate that large volumes of gas can be safely and permanently stored.

J. M. Carcione (✉) · D. Gei · S. Picotti
Istituto Nazionale di Oceanografia e di Geofisica Sperimentale (OGS), Borgo Grotta Gigante 42c,
34010 Sgonico, Trieste, Italy
e-mail: jcarcione@inogs.it

M. S. Misnan · M. R. A. Rashidi · Z. A. A. Bakar
PETRONAS Research Sdn. Bhd., Bandar Baru Bangi,
Malaysia

Z. Z. T. Harith · N. H. S. Bahri · N. Hashim
AEM Energy Solutions Sdn. Bhd., Kuala Lumpur,
Malaysia

Reservoir and overburden rock porosity and permeability are important in hydrocarbon production and during the last 30 years, the success of CO_2 storage relies on a proper estimation of these properties in the reservoir, as well as on the seal caprock and overburden to avoid possible leakages (Picotti et al. 2012; Savioli et al. 2016; Fang et al. 2017). Low permeability is required in this case and strongly depends on grain size and sediment compaction. Fine-grain sediments, mud and its lithified versions (mudstone and shale), form approximately 70 % of the sedimentary basins. The permeability of shales is several orders of magnitude lower than that of coarser grain rocks, such as sandstones and carbonates (Ngo et al. 2018). Actually, there are many factors that control fluid-flow properties in porous media (e.g., Singh et al. 2015), which are a complex combination of wettability, interaction of molecular forces, pore-size range and distribution, permeability, gravity, capillary pressure, location in the reservoir, temperature and pressure. In this work, we focus on how permeability is affected by clay. Shales and even sandstone with a moderate amount of clay particles (shaley sandstones) control the fluid flow in the underground. Clay particles can reduce the permeability by increasing the tortuosity and blocking the pore throats.

Evaluating the permeability of mudstone or shale is a challenging task. Pressure-pulse decay is one of the methods to deal with extremely low permeability values, however, it is rather expensive, and the value is often questionable, due to tedious sample preparation process. Often, these values must be calculated/estimated with what is available. In this work, the permeability of the overburden shale layer is estimated from a modification of the conventional wireline logs equations.

In hydrocarbon exploration, the focus is normally given in getting accurate flow properties of the reservoir, with very minimal attention to the overlaying sediments, and often the permeability of the shale is assumed to be zero (no flow material). This approach might be correct for modeling hydrocarbon production, but it is not the case for CO_2 storage. Permanent storage is the main objective, thus even a very small permeability should be considered to avoid any possibility of leakage. An essential quantity to evaluate permeability is porosity. The equations proposed here are not standard practice in log interpretation, but they are used in seismic exploration, so their validity is guaranteed. Classical log interpretation misses the shale effect, since it deals with reservoirs, not the overburden, constituted mainly of shales. The proposed equations to obtain the porosity from densities and traveltimes are novel. Then, we use the Voigt–Reuss–Hill and Gassmann equations to verify the reliability of the porosity estimation with the sonic log, which provides better estimates than the density-derived porosity. This is also confirmed by comparison to porosity obtained from the neutron log.

A depleted carbonate field offshore Malaysia has been identified as a possible storage site for carbon dioxide (Masoudi et al. 2011). The field is located north of Central Luconia Province in the Sarawak Basin, East Malaysia. Central Luconia is the major gas contributor, containing 60% of the Malaysian gas reserves. It extends for some 240 × 240 km and is covered by the South China sea, which is up to 80 m deep. More than 200 carbonate platforms have been mapped and out of those 60 have been drilled so far in the area of Sarawak, Malaysia. The corals and coralline red algae are the chief contributors for the growth of these carbonate platforms, where the production is controlled by coralline red algae. More information about the geological characteristics of the area can be found in Janjuhah et al. (2017).

The reservoir is approximately 2 km below sea-level where the water depth is approximately 120 m. It is essential to predict possible migration patterns of the CO_2 in the overburden, which may give rise to dangerous leakages to the ocean. Knowing clay content is required to obtain reliable values of permeability, since it is strongly correlated with the grain and pore size distributions. The term "clay" is defined here as the volume fraction of particles less than 4 μm in diameter, and not specifically to intrinsic clay minerals. Therefore it is a synonymous of shale particles. This innovative approach was tested on one of the CO_2 storage candidates in Malaysia. A depleted carbonate field offshore Malaysia has been identified as storage site for carbon dioxide (Masoudi et al. 2011).

2 Methodology

We modify the conventional density/porosity and transit time/porosity relations to include the effects of shale on the calculation of the overburden porosity. Then, we verify the procedure by using the Krief–Gassmann equations to obtain the P-wave velocity from porosity, either from the density-log or from sonic-log derived porosities. The fact that the latter estimation is the best is confirmed by comparison to porosity obtained from the neutron log. To compute permeability, we use Kozeny–Carman type equations (Kozeny 1927; Carman 1961; Tiab and Donaldson 2012) based on grain size (clay content) and tortuosity.

2.1 Clay content

The shale volume is first obtained with the classical linear relation,

$$C = \frac{\gamma - \gamma_{\min}}{\gamma_{\max} - \gamma_{\min}} \tag{1}$$

(Ellis and Singer 2008), where γ is the gamma-ray value in API, $\gamma_{\min}$ is the minimum value (pure sandstone) and $\gamma_{\max}$ is the maximum value (pure shale). We also perform calculations using the Stieber equation (Stieber 1970) to obtain the clay content, i.e.,

$$C = \frac{\mathrm{IGR}}{3 - 2\ \mathrm{IGR}}, \quad \mathrm{IGR} = \frac{\gamma - \gamma_{\min}}{\gamma_{\max} - \gamma_{\min}}. \tag{2}$$

2.2 Porosity

First, let us obtain the porosity from the density log. In the scientific community, porosity ϕ is often calculated from this log by means of the following equation:

$$\phi = \frac{\rho - \rho_s}{\rho_f - \rho_s} - C\left(\frac{\rho_c - \rho_s}{\rho_f - \rho_s}\right) \tag{3}$$

(Crain 2018), where ρ_s and ρ_c are the quartz-silt (clastic or sand) and shale-particle densities, respectively, and ρ_f is the fluid (brine) density. Here, ρ_c is the log reading at 100% shale, i.e., $C = 1$. At this value, $\rho = \rho_c$ and $\phi = 0$, since it is implicitly assumed that shale has zero porosity. This equation corrects the density-log total porosity (first term of the r.h.s) to its effective value by removing the shale contribution. As a consequence, if this effective porosity is used in the Kozeny–Carman equation to obtain the permeability, the result for shales is zero, and this is not realistic.

We follow a different approach, which is based on finite porosity values of the shale component, where porosity of the quartz-silt and shale components contribute to the total porosity, i.e., there is no such concept of effective porosity. Bulk density is

$$\rho = (1 - \phi)\rho_g + \phi\rho_f, \tag{4}$$

where ϕ is the porosity and ρ_g is the grain density. This depends on the clay content C as $\rho_g = (1 - C)\rho_s + C\rho_c$, where here ρ_c is the mineral density of the shale. Therefore,

$$\rho = (1 - \phi)[(1 - C)\rho_s + C\rho_c] + \phi\rho_f \tag{5}$$

and from Eqs. (4) and (5), we obtain the porosity as

$$\phi = \frac{\rho - \rho_g}{\rho_f - \rho_g} = \frac{\rho - \rho_s + C(\rho_s - \rho_c)}{\rho_f - \rho_s + C(\rho_s - \rho_c)}. \tag{6}$$

Here $\phi = (\rho - \rho_c)/(\rho_f - \rho_c)$ when $C = 1$. The difference between porosity at 100% quartz-silt and 100% shale is $\Delta\phi = (\rho_s - \rho_c)/(\rho_s - \rho_f)$ and this difference increases for decreasing ρ_c. This approach is based on the fact that shale has porosity and that the observed small permeability is due to the effects of grain size, specific surface area and tortuosity. When the grain size decreases and the specific surface area increases (pore size decreases), permeability decreases (e.g., Carcione et al. 2018).

An expression similar to Eq. (3) is used to obtain porosity from the sonic log by replacing ρ_i with the transit time t_i. Here, to incorporate the shale contribution, we obtain porosity from the sonic log by using the time-average Eq. (Carcione 2014). The transit time is

$$t = (1 - \phi)t_g + \phi t_f, \tag{7}$$

where t_g and t_f are the transit times in the grain and fluid, respectively, Since the solid part consists of quartz-silt and shale, we have

$$t_g = (1 - C)t_s + Ct_c, \tag{8}$$

where the subindex s and c refer to quartz-silt and shale grains, respectively. From Eq. (7), we obtain the porosity as

$$\phi = \frac{t - t_g}{t_f - t_g} = \frac{t - t_s + C(t_s - t_c)}{t_f - t_s + C(t_s - t_c)}. \tag{9}$$

One method to check the reliability of the porosity estimation is to obtain the P-wave velocity from physical grounds and compare it to the actual sonic-log velocity. The approach that we use here is the Krief–Gassmann model, where the dry- and wet-rock moduli are obtained with Krief and Gassmann equations, respectively (e.g., Carcione et al. 2006). The Krief dry-rock bulk moduli are

$$K_m = K_g \phi (1 - \phi)^{A/(1-\phi)} \quad \text{and} \quad \mu_m = \mu_G = \frac{3}{5} K_m, \tag{10}$$

where K_g is the grain bulk modulus, A is a constant and the shear modulus is that of a Poisson medium (the Lamé constants are equal); μ_G is the wet-rock shear modulus (second Gassmann equation).

We assume that the composite bulk modulus of the grains is given by the Voigt–Reuss–Hill (VRH) average. The Voigt and Reuss averages are iso-strain and iso-stress approximations, respectively (the stress and strain are unknown and are expected to be non-uniform). The VRH estimates were found in most cases to have an accuracy comparable to those obtained by more sophisticated techniques such as self-consistent schemes and are valid for complex rheologies such as general anisotropy and arbitrary grain topologies. It gives values similar to the Hashin-Shtrikman average and the equation is simpler (Picotti et al. 2018). We have

$$K_g = \frac{1}{2}(K_V + K_R), \tag{11}$$

where

$$K_V = (1 - C)K_s + CK_c \quad \text{and} \quad K_R^{-1} = \frac{1 - C}{K_s} + \frac{C}{K_c}, \tag{12}$$

where K_s and K_c are the quartz-silt and shale bulk moduli, respectively. Gassmann bulk modulus is then

$$K_G = \frac{K_g - K_m + \phi K_m \left(K_g / K_f - 1\right)}{1 - \phi - K_m / K_g + \phi K_g / K_f} \tag{13}$$

(e.g., Carcione 2014). The effective (bulk) density is given by the arithmetic average:

$$\rho = (1 - \phi)\rho_g + \phi \rho_f = (1 - \phi)[(1 - C)\rho_s + C\rho_c] + \phi \rho_f. \tag{14}$$

Then, the P-wave velocity is

$$v_P = \sqrt{\frac{K_G + 4\mu_G/3}{\rho}}. \tag{15}$$

2.3 Permeability

We estimate permeability by using three models (Carcione et al. 2018). The first model (Model 1) assumes that a medium composed of sand and shale grains of total porosity ϕ and clay content C has a permeability given by

$$\kappa = \left\{ \frac{(1 - \phi)^2}{a\phi^3} \left[(1 - C)^2 + C^2 b^2 \right] \right\}^{-1}, \tag{16}$$

where $a = r_s^2/45$ and $b = r_s/r_c$, where r_s and r_c are the radii of the sand and shale particles, respectively (Carcione et al. 2000). Parameters a and b have to be used as free parameters obtained from calibration of available data. These parameters contain information about the geometrical characteristics of the rock frame, such as the mean radius of the grains and the effective tortuosity $\mathcal{T}$ of the sand/shale frame network. Actually the factor 45 has been obtained in Carcione et al. (2018) as 18 $\mathcal{T}$, with $\mathcal{T} = 2.5$, which is an idealization for spherical grains, but one cannot expect to fit real data by considering a and b a result of such an ideal assumption.

A classical model of permeability (Model 2) is given in terms of tortuosity,

$$\kappa = \frac{r_g^2 \phi^3}{18\mathcal{T}(1 - \phi)^2}, \tag{17}$$

where

$$r_g = Cr_c + (1 - C)r_s \tag{18}$$

is the average grain radius and $\mathcal{T}$ is the tortuosity given by

$$\mathcal{T} = 1 - 0.5\left(1 - \frac{1}{\phi}\right). \tag{19}$$

However, this tortuosity factor is most probably too low for shales and this property has to be used as a fitting parameter. Indeed, Backeberg et al. (2017) (their Fig. 5) report values for shales as high as 1000. Hence, the permeability values obtained here have to be scaled down by a factor 100 or more.

Another approach to obtain permeability is based on specific surface area s (Model 3), if available from laboratory measurements. In this case, we avoid using the clay content. Permeability is given by

$$\kappa = \frac{\phi^3}{2s^2\mathcal{T}} \tag{20}$$

(Carcione et al. 2018).

3 Results

In this section, we obtain clay content, porosity and permeability at two well locations. We consider a geophysical dataset acquired for a hydrocarbon field located north of Central Luconia Province in the Sarawak Basin, East Malaysia. Figure 1 shows seven main surfaces characterizing the 3D geological model of the study area and the location of 2 wells considered in this study. The analysis regards the formations above the carbonate reservoir (in red) (mainly low permeability shales). We focus on well XYZ-2 and XYZ-3; the log profiles of the first well are shown in Fig. 2. The depth of investigation ranges from 800 m below the ocean bottom to approximately 2 km depth. We proceed to make the calculations using the bulk density, gamma ray and sonic transit-time profiles exclusively, i.e., original—unprocessed—logs.

3.1 Well XYZ-2

The gamma-ray log is represented in Fig. 3a and we use Eq. (1) to obtain the clay content. From Fig. 3a we consider $\gamma_{\min} = 50$ and $\gamma_{\max} = 120$ (the actual values are 50 and 139), giving the shale-content profile shown in Fig. 3b. Default values in the literature are $\gamma_{\min} = 15$ and $\gamma_{\max} = 115$ (Crain 2018). Other laws other than the linear one could be considered, such as the Larionov, Stieber and Clavier equations (Larionov 1969; Clavier et al. 1971; Stieber 1970). Below, the Stieber relation is considered as well. It is shown that the results are not much different.

We consider the typical densities $\rho_s = 2650$ kg/m^3, $\rho_c = 2600$ kg/m^3 and $\rho_f = 1040$ kg/m^3 (brine). The log transit times are actually slownesses given in μs/ft $= 3.28$ µs/m. We assume that the bulk moduli of the sand and shale grains are $K_s = 40$ GPa, and $K_c = 20$ GPa, respectively. Moreover, the fluid bulk modulus is $K_f = 2.25$ GPa. Assuming a Poisson medium (the Lamé constants are equal), the P-wave velocity for the three phases is $3\sqrt{K/(5\rho)}$. These values of the bulk moduli and density correspond to

Fig. 1 Location of the three wells offshore Malaysia. The carbonate reservoir is indicated in red color. Depth z is in meters

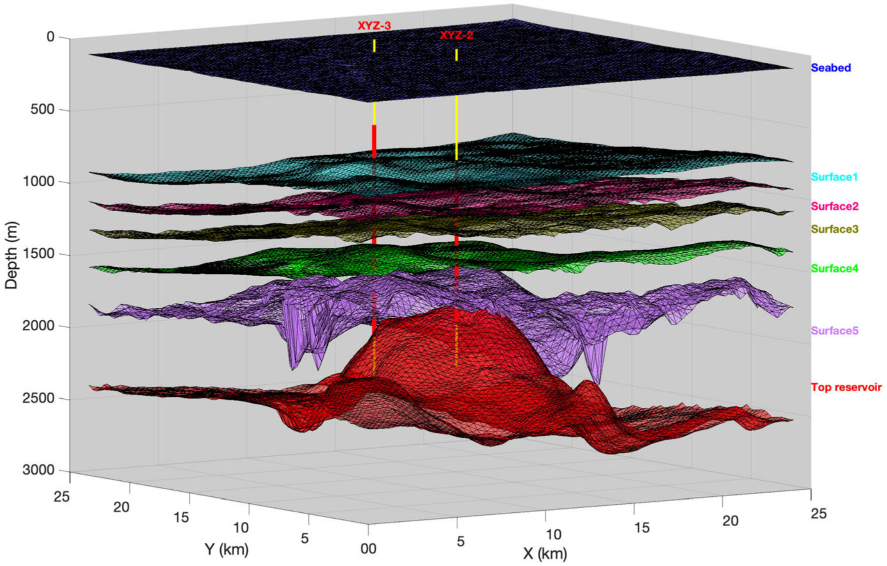

Fig. 2 Log profiles of well XYZ-2

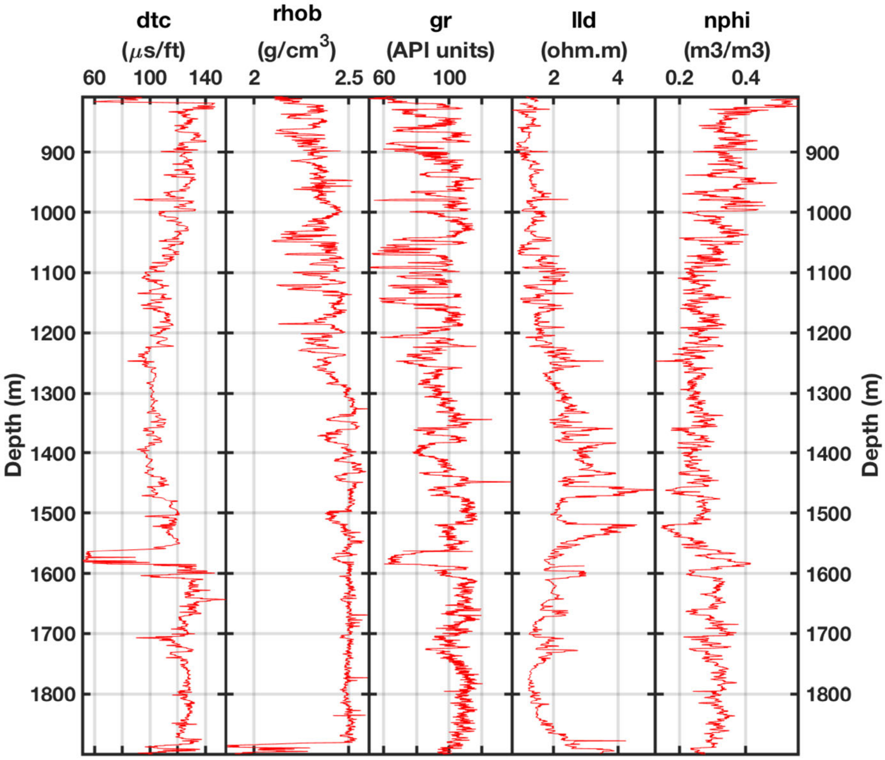

the following transit times, $t_s = 58$ µs/ft, $t_f = 207$ µs/ft and $t_c = 82$ µs/ft, which correspond to the P-wave velocities 5212 m/s, 1471 m/s and 3721 m/s, for sand, brine and clay, respectively (typical values to process sonic logs). We obtain the porosity profiles shown in Fig. 4 (from bulk density and transit times). As can be seen, the two profiles are very different, mainly below 1.4 km depth, where the sonic porosity has much higher values.

To be consistent, we consider that the K_s, K_c, ρ_s, ρ_c and ρ_f values are those indicated above to obtain the porosity from the sonic and density logs, that $A = 3.5$ (a typical value in many basins worldwide), and that the density values are those to obtain the porosity from the density log. Figure 5 compares the velocities obtained with Eq. (15), considering the sonic-log (black) and density-log (red) porosities with the actual sonic-log values (blue). As can be appreciated, the porosity derived from the sonic log yields a velocity which coincides with the actual sonic-log velocity, unless in the range 1.2–1.5 km depth. This can be due to the assumption of a Poisson medium, but we do not have data to obtain the S-wave velocity. Another possibility is the use of a different equation to obtain the clay content (see below). The decrease in velocity below 1.5 km depth agrees with the porosity increase in that range (see Fig. 4). This analysis poses doubts about the reliability of the density log. Of course, the density used in Eq. (15) to obtain the velocity using the density-estimated porosity is taken from the density log. Instead, to compute the velocity with the sonic log-estimated porosity we use the bulk density given by Eq. (14). However, the correct velocity is obtained with the sonic-estimated porosity and density. These two density profiles are shown in Fig. 6, where the black curve corresponds to the last quantity.

Another partial confirmation is to compare the porosities obtained from the density and sonic logs with the neutron porosity (Fig. 2, panel 5). Figure 7 shows the three curves, where it can be seen that the sonic porosity coincides with the neutron porosity. In this case, the neutron porosity should not be corrected for the shale effect (e.g., Ellis and Singer 2008), since this correction implicitly assumes that the shale porosity is zero. These types of shale corrections apply to clastic reservoirs but not to shale formations. Methodologies that remove the shale effect are implemented because shales cannot produce

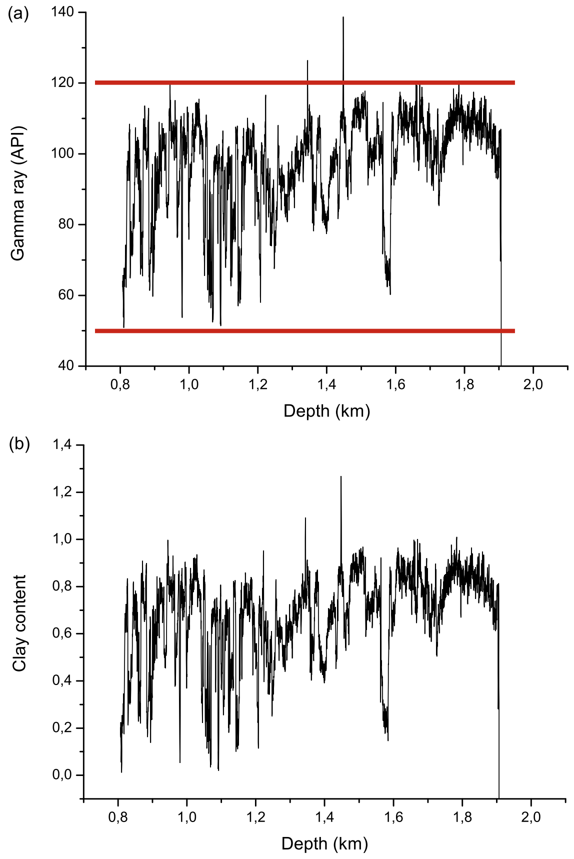

Fig. 3 Gamma-ray log (**a**) and clay content (**b**) of well XYZ-2. The red lines indicate the minimum and maximum—interpreted—gamma-ray values used in the calculation of the clay content

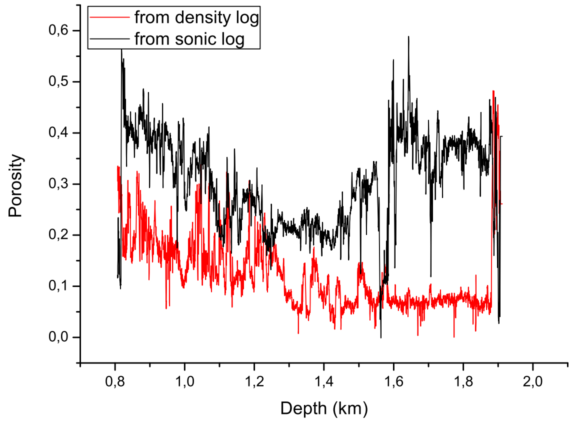

Fig. 4 Porosity profiles obtained from the density (red) and sonic (black) logs for well XYZ-2. Anomalous spikes in the sonic log generate anomalous values of porosity

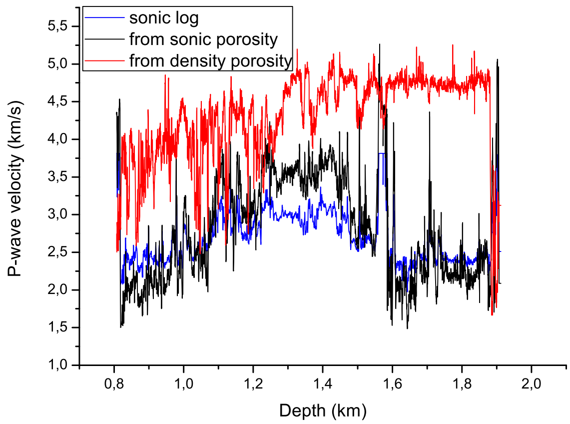

Fig. 5 P-wave velocity for well XYZ-2 obtained with the Krief–Gassmann model based on the sonic porosity (black) and the density porosity (red) compared to the sonic-log velocity (blue)

hydrocarbons and their contributions to the measurements is subtracted from the total porosity to obtain the so-called effective porosity, solely related to the quartz-silt component of the rock.

Let us obtain permeability from Eqs. (16), (17) and (20). The pore sizes in shales are in the range of 1–100 nm, with typical specific surface areas of $s_m = 14\,\mathrm{m}^2/\mathrm{g}$ (mass normalized) (see Kuila and Prasad 2013, Table 2, Pierre shale values). The volume normalized surface area is $s = s_m\rho$, where ρ is the density of the shale. For $\rho = 2.3$ g/cm^3, we have $s = 32 \times 10^6$ 1/m. For spherical grains, surface area and grain size are related as $s = 3(1-\phi)/r_g$ (Carcione et al. 2018).

The radii of the sand and shale particles assumed here are $r_s = 30\,\mu\mathrm{m}$ and $r_c = 0.05\,\mu\mathrm{m}$, respectively, and the specific surface area for Model 3 is that of Pierre shale. Figure 8 compares the results of the three models, which are similar. Re-scaled with realistic tortuosity values (factor 100), we obtain permeabilities of the order of 10 nano-darcies.

Alternatively, we can use Stieber equation (2) to obtain the clay content. The results are shown in Figures 9, 10, 11, 12, 13 and 14. Basically, the differences with the linear law (1) are that the clay content estimated with the Stieber equation is smaller. On the other hand, the fit between the P-wave velocity derived from the sonic porosity and the actual one is better than above.

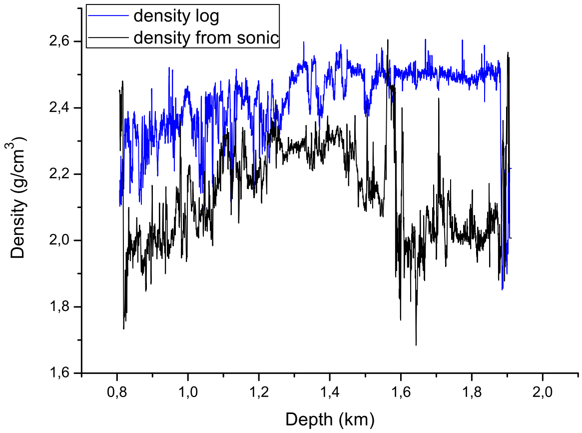

Fig. 6 Density profiles obtained from the sonic log (black) compared to the reported density profile (blue) for well XYZ-2

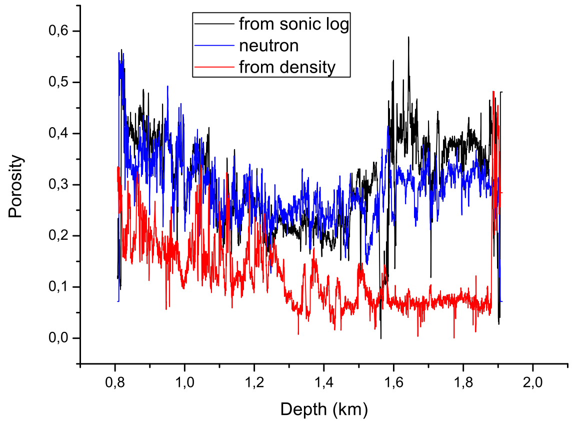

Fig. 7 Comparison of the density and sonic porosities with the neutron porosity

3.2 Well XYZ-3

Figure 15 shows the log profiles of well XYZ-3. The clay content profile is obtained with the Stieber equation (2). Gamma ray and clay content are shown in Fig. 16. We obtain the porosity profiles shown in Fig. 17 (from bulk density and transit times). As can be seen, the two curves are quite different. Figure 18 compares the velocities obtained from the sonic (black) and density (red) logs with the actual one (blue). To be consistent, we have used the same properties and parameters to process well XYZ-2. It is evident that the velocity derived from the sonic porosity agrees with the actual velocity. The two density profiles are shown in Figs. 19 and 20 compares

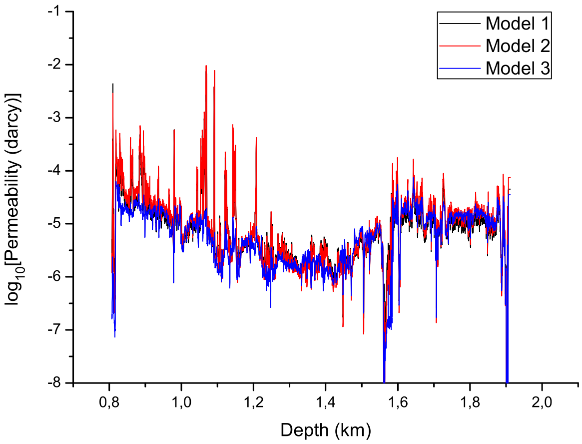

Fig. 8 Permeability profiles for well XYZ-2 obtained from the sonic-log porosity, corresponding to the three models

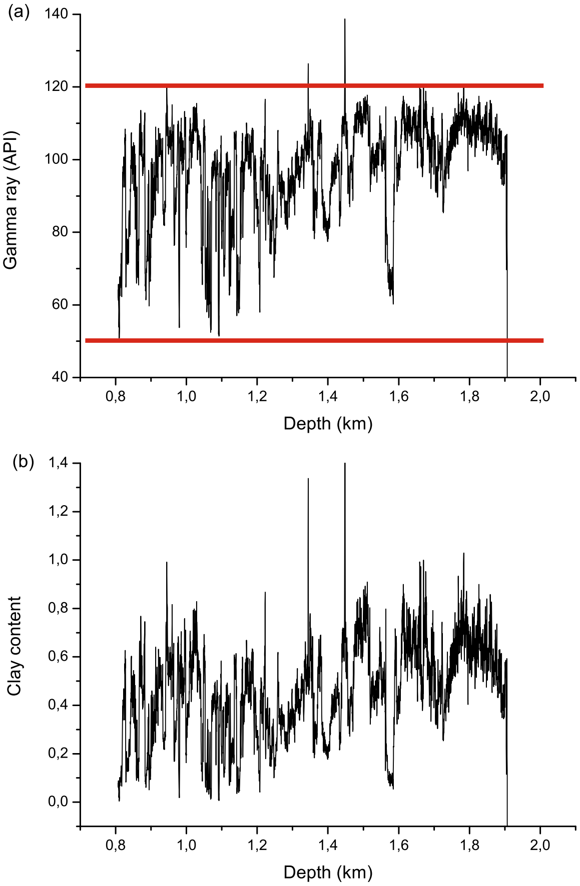

Fig. 9 Gamma-ray log (**a**) and clay content (**b**) of well XYZ-2. The red lines indicate the minimum and maximum—interpreted—gamma-ray values used in the calculation of the clay content. The calculations are based on Stieber equation (2)

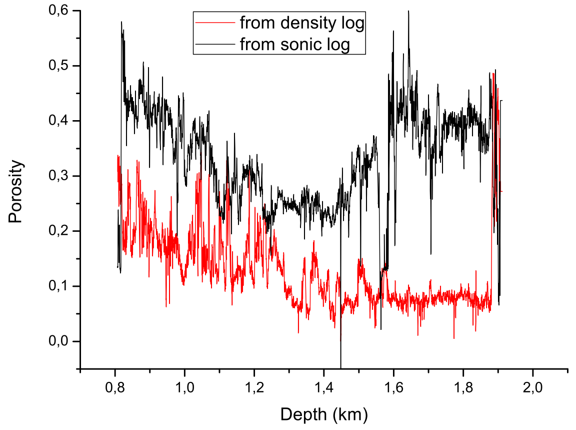

Fig. 10 Porosity profiles obtained from the density (red) and sonic (black) logs for well XYZ-2. Anomalous spikes in the sonic log generate anomalous values of porosity. The calculations are based on Stieber equation (2)

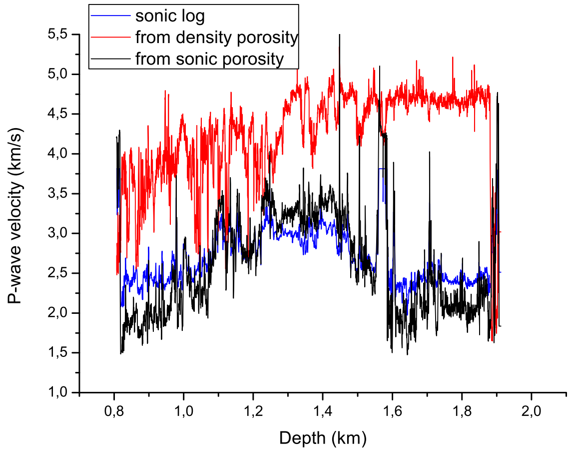

Fig. 11 P-wave velocity for well XYZ-2 obtained with the Krief–Gassmann model based on the sonic porosity (black) and the density porosity (red) compared to the sonic-log velocity (blue). The calculations are based on Stieber equation (2)

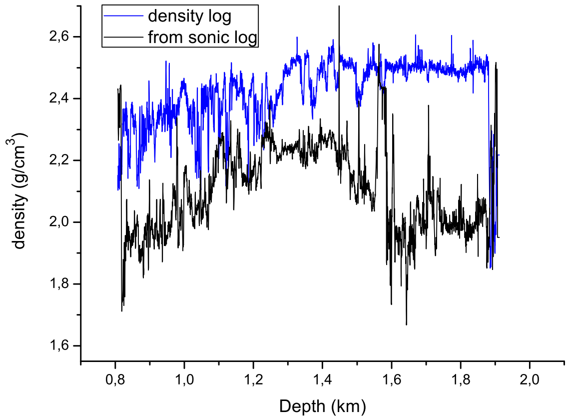

Fig. 12 Density profiles obtained from the sonic log (black) compared to the reported density profile (blue) for well XYZ-2. The calculations are based on Stieber equation (2)

the results of the three permeability models. Model 3 yields smaller permeabilities, since these are obtained for pure shale (specific surface area of Pierre shale in this case).

An effect that it is worth studying in the future is the sorption of CO_2 by smectite. In particular, this may lead to swelling, closure of fractures and the reduction of fracture apertures, thereby affecting the permeability of the shale. An initial study has been performed by Busch et al. (2016), that can be extended to the permeability models presented in the present work.

Fig. 13 Comparison of the density and sonic porosities with the neutron porosity. The calculations are based on Stieber equation (2)

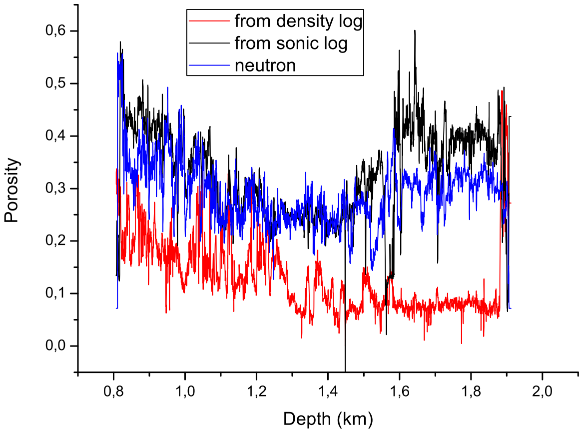

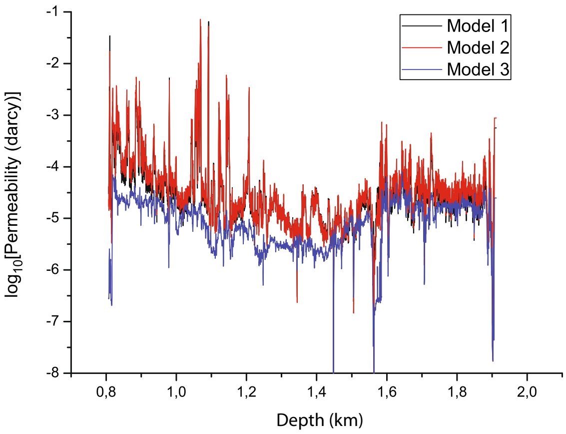

Fig. 14 Permeability profiles for well XYZ-2 obtained from the sonic-log porosity, corresponding to the three models. The calculations are based on Stieber equation (2)

4 Conclusions

Well-log processing methodologies that remove the shale effect are implemented in reservoir geophysics, because shales cannot produce hydrocarbons and their contributions to the measurements is subtracted from the total porosity to obtain the so-called effective porosity, solely related to the quartz-silt component of the reservoir. This correction implicitly assumes that the shale porosity (and permeability) is zero, so that it applies to clastic reservoirs but not to shale formations. When the target is the overburden and not the reservoir, we have to consider that shales have a non-zero porosity and a finite permeability even if the flow rates are several orders of magnitude smaller than those in sandstones. In CO_2 monitoring, we are concerned with fluid flow at the scale of years and decades, not days and months as in reservoir production. We show that the sonic log gives a better estimate of porosity that honours the P-wave velocity. The verification is performed by using the Krief–Gassmann equations to obtain the P-wave velocity from porosity. It is verified that the sonic porosity coincides

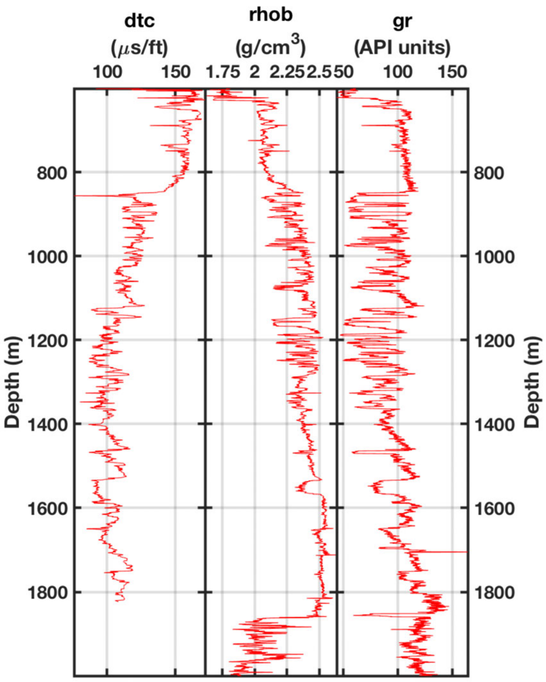

Fig. 15 Log profiles of well XYZ-3

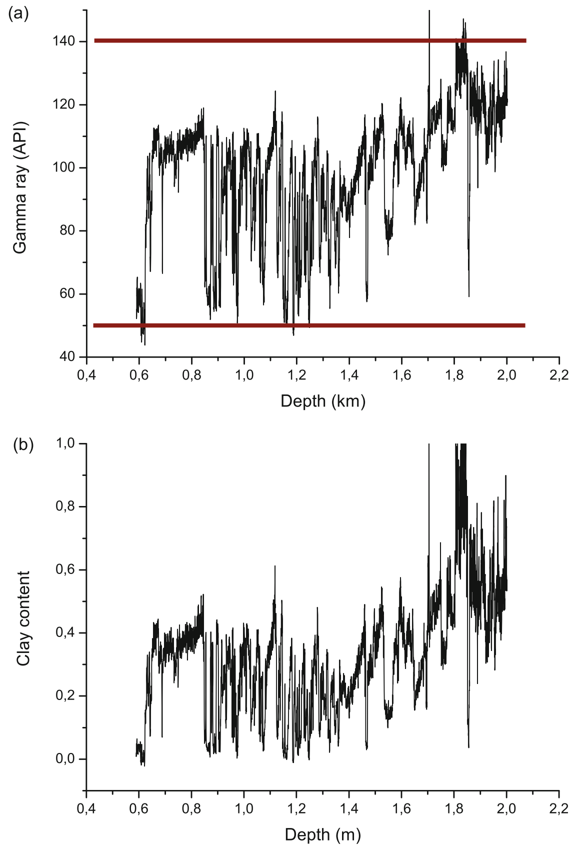

Fig. 16 Gamma-ray log (**a**) and clay content (**b**) of well XYZ-3. The bars indicate the minimum and maximum—interpreted—gamma-ray values used in the calculation of the clay content

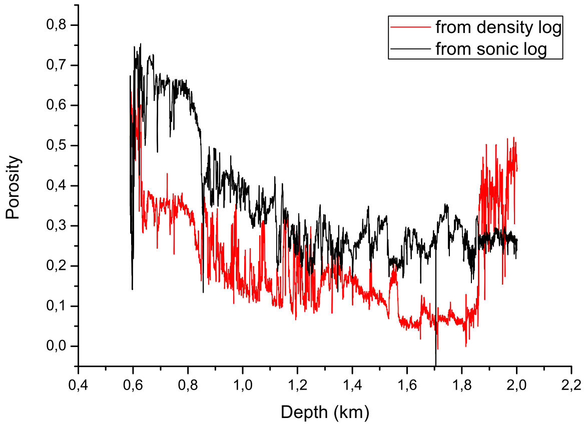

Fig. 17 Porosity profiles obtained from the density (red) and sonic (black) logs for well XYZ-3

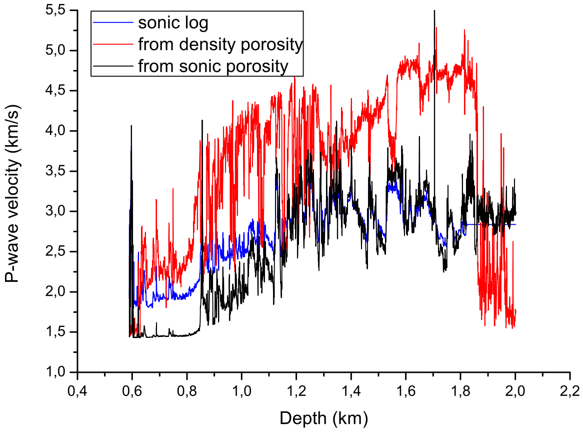

Fig. 18 P-wave velocity for well XYZ-3 obtained with the Krief–Gassmann model based on the sonic porosity (black) and the density porosity (red) compared to the sonic-log velocity (blue)

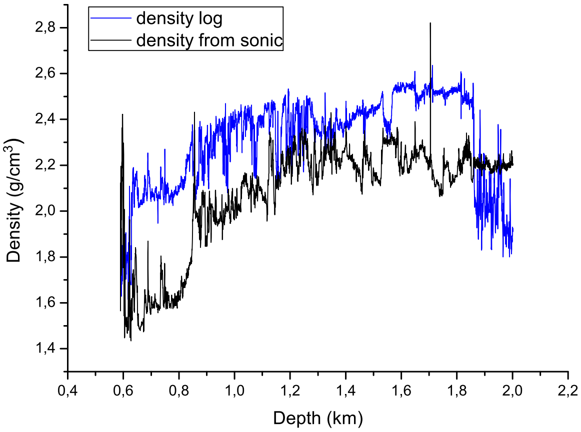

Fig. 19 Density profiles obtained from the sonic log (black) compared to the reported density profile (blue) for well XYZ-3

with the neutron porosity. Permeability is then obtained with three different models, based on grain size, tortuosity and surface area, respectively.

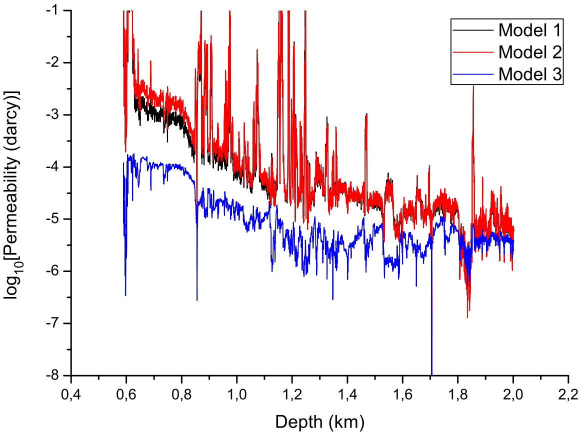

Fig. 20 Permeability profiles for well XYZ-3 obtained from the sonic-log porosity, corresponding to the three models

Acknowledgements This work was funded by Petronas.

Compliance with ethical standards

Conflict of interest On behalf of all authors, the corresponding author states that there is no conflict of interest.

References

Backeberg NR, Iacoviello F, Rittner M, Mitchell TM, Jones AP, Day R, Wheeler J, Shearing PR, Vermeesch P, Striolo A (2017) Quantifying the anisotropy and tortuosity of permeable pathways in clay-rich mudstones using models based on X-ray tomography. Sci Rep 7:14838. https://doi.org/10.1038/s41598-017-14810-1

Brown K, Whittaker S, Wilson M, Srisang W, Smithson H, Tontiwachwuthikul P (2017) The history and development of the IEA GHG Weyburn-Midale CO_2 monitoring and storage project in Saskatchewan, Canada (the world largest CO_2 for EOR and CCS program). Petroleum 3:3–9

Busch A, Bertier P, Gensterblum Y, Rother G, Spiers CJ, Zhang M, Wentinck HJM (2016) On sorption and swelling of CO_2 in clays. Geomech Geophys Geo-energ Geo-resour 2(2):111–130

Carcione JM (2014) Wave fields in real media. Theory and numerical simulation of wave propagation in anisotropic, anelastic, porous and electromagnetic media, Elsevier (Third edition, extended and revised)

Carcione JM, Gurevich B, Cavallini F (2000) A generalized Biot–Gassmann model for the acoustic properties of shaley sandstones. Geophys Prosp 48:539–557

Carcione JM, Picotti S, Gei D, Rossi G (2006) Physics and seismic modeling for monitoring CO_2 storage. Pure Appl. Geophys. 163:175–207

Carcione JM, Gei D, Yu T, Ba J (2018) Effect of clay and mineralogy on permeability. Geophys Pure Appl. https://doi.org/10.1007/s00024-019-02117-3

Carman PC (1961) L' écoulement des gaz á travers les milieux poreux, Bibliothéque des Sciences et Techniques Nucléaires, Presses Universitaires de France, Paris

Clavier C, Hoyle W, Meunier D (1971) Quantitative interpretation of thermal neutron decay time logs: Part I. Fundamentals and techniques. J Pet Technol 23:743–755

Crain ER (2018) Crain's petrophysical handbook. www.spec2000.net

Ellis DV, Singer JM (2008) Well logging for earth scientists. Springer, Berlin

Fang Y, Wang C, Elsworth D, Ishibashi T (2017) Seismicity-permeability coupling in the behavior of gas shales, CO_2 storage and deep geothermal energy. Geomech Geophys Geo-energ Geo-resour. https://doi.org/10.1007/s40948-017-0051-9

Janjuhah HT, Salim AMA, Ghosh DG (2017) Sedimentology and reservoir geometry of the Miocene carbonate deposits in Central Luconia, Offshore, Sarawak, Malaysia. J Appl Sci 17(4):153–170

Kozeny J (1927) Über kapillare leitung desWassers im Boden: Sitzungsberichte derWienerAkademie desWissenschaften 136:271–306

Kuila U, Prasad M (2013) Specific surface area and pore-size distribution in clays and shales. Geophys Prosp 61:341–362

Larionov VV (1969) Radiometry of boreholes (in Russian). NEDRA, Moscow

Masoudi R, Jalil MAA, Press D, Lee K-H, Phuat C, Anis L, Darman N, Othman M (2011) An integrated reservoir simulation-geomechanical study of feasibility of CO_2 storage in M4 carbonate reservoir, Malaysia, International Petroleum Technology ConferenceIPTC 15029

Ngo VT, Lu VD, Le VM (2018) A comparison of permeability prediction methods using core analysis data for sandstone and carbonate reservoirs. Geomech Geophys Geo-energ Geo-resour 4(2):129–139

Picotti S, Carcione JM, Gei D, Rossi G, Santos JE (2012) Seismic modeling to monitor CO_2 geological storage—the Atzbach-Schwanenstadt gas field. J Geophysics Res Solid Earth 117(6):B06103. https://doi.org/10.1029/2011JB008540

Picotti S, Carcione JM, Ba J (2018) Rock-physics templates for seismic *Q*. Geophysics 84(1):MR13–MR23

Savioli GB, Santos JE, Carcione JM, Gei D (2016) A model for CO_2 storage and seismic monitoring combining multiphase fluid flow and wave propagation simulators. The Sleipner-field case. Comput Geosci. https://doi.org/10.1007/s10596-016-9607-y

Singh KK, Singh DN, Ranjith PG (2015) Laboratory simulation of flow through single fractured granite. Rock Mech Rock Eng 48:987–1000

Stieber SJ (1970) Pulsed neutron capture log evaluation—Louisiana Gulf Coast: Society of Petroleum Engineers Annual Fall Meeting Proceedings, SPE 2961

Tiab D, Donaldson EC (2012) Petrophysics. Theory and practice of measuring reservoir rock and fluid transport properties, 3rd edn. Gulf Professional Publishing